Platinum supported on pristine and nitrogen doped bowl-like broken hollow carbon spheres as oxygen reduction reaction catalysts

Victor Mashindi[1], Pumza Mente[1], Nobuhle Mpofu[3], Tumelo N. Phaahlamohlaka[1], Ofentse Makgae[2], Angus I. Kirkland[2], Roy Forbes[1], Kenneth I. Ozoemena[1], Pieter B. Levecque[3] and Neil J. Coville[1]*,

[1]Molecular Sciences Institute, School of Chemistry, University of the Witwatersrand, Johannesburg 2050, South Africa

[2] Department of Materials, University of Oxford, Parks Road, Oxford, OX1 3PH, UK

[3] HySA Catalysis Centre of Competence, Catalysis Institute, Department of Chemical Engineering, University of Cape Town, 7701, South Africa

*Prof Neil Coville. E-mail: neil.coville@wits.ac.za. Tel: +27 (0) 11 717 6738.

Abstract

The development of active and durable proton exchange membrane fuel cell catalysts with high loading (ca. 40%) is critical for the commercialization of hydrogen fuel cells. Herein we report on the synthesis of a novel Pt/C catalyst using a novel bowl-like broken hollow carbon sphere (and N doped sphere) support (carbon shell thickness ~ 4.6 nm). Highly dispersed Pt nanoparticles (d_{Pt} ~ 4 nm) were deposited on both supports and within the carbon shell. The Pt particles in the pores were exposed on both sides of the shell, while the shell porosity ensured pore confinement of the Pt. Both catalysts exhibited high electrochemical surface areas (60–65 m^2 g^{-1}) and cycling durability (6000 cycles) that was superior to a commercial benchmark Pt/C catalyst. These studies indicate that high loadings of confined small Pt particles on both sides of thin interconnected carbons can lead to high oxygen reduction reaction activities and durability.

Keywords: metal-support interactions; broken bowl-like carbon; oxygen reduction reaction; nitrogen doping; pore confinement.

1. Introduction

The proton exchange membrane fuel cell (PEMFC) is the fuel cell of choice for applications in transport due to its light weight, fuel efficiency, high power density and relatively low noise

production [1-2]. When the hydrogen fuel is sourced from solar electrolysis of water, the PEMFCSs are green and sustainable due to their neutral carbon footprint. Compared to other catalysts, the Pt used in PEMFC reactions can also have a lower overpotential for both the anode hydrogen oxidation reaction (HOR) and cathode oxygen reduction reaction (ORR) [3]. Hence, even though it has a high cost, Pt is still the catalyst of choice in the above reactions.

A requirement of any new PEMFC catalyst, by the USA Department of Energy 2020 targets, is that it must have a mass activity > 0.44 A mg^{-1}, and more than 5000 h of cycling durability [4]. A number of research efforts have thus been made to sustain and enhance Pt catalysts in the fuel cell reactions. One is to replace expensive Pt by metals like Fe and Ni which are known to exhibit good ORR properties. However, their mass specific activity (MA) and surface area specific activity (SA) are not as high as found for Pt [5-6]. Therefore, for improved ORR activity Fe, Ni and other transition metals have been alloyed with Pt to produce catalyst systems with MA and SA more than 2-fold better than for the Pt catalysts [7-10]. However, the alloys of Pt and the transition metals suffer from low durability caused by the leaching in acid media of the transition metals in a fuel cell [11].

Another approach used to enhance the activity of Pt is to use an appropriate support. To date, conventional ORR catalysts have been Pt nanoparticles supported on high surface area and conductive carbons or conductive metal oxides including Sb doped SnO_2 [12]. However, the metal oxide support can be expensive, possess low conductivity, low porosity and also low surface area resulting in poor dispersion of the active Pt or Pt alloy catalysts. This can, in some cases, also lead to low SA and MA values compared to Pt deposited on the standard conductive and porous C supports. For these reasons, C is currently the support of choice. However, during the start-up of the fuel cell cathode potentials can reach above 1.5 V vs. RHE, causing degradation of both the Pt catalysts and the C supports [13].

Even though high surface area graphitic carbons are characterized by low durability in fuel cells, structured carbon supports are known to exhibit characteristics that can be exploited to generate suitable Pt or Pt-alloy catalyst supports for fuel cell applications [14]. The low cost, high BET surface area, arrays of mesopores and micropores, electronic conductivity, high thermal stability, ability to be moulded into various shapes and allotropes, light weight for mobile applications and mechanical durability makes structured carbons suitable candidates for ORR catalysis. In-situ or post-synthesis functionalization of these structured carbons

modifies the surface chemistry of these supports, sometimes resulting in better tethering of the Pt to the support and subsequently promoting durability [15].

In this study small diameter and thin graphitic shell bowl-like broken hollow C spheres (BHCSs) and their N doped counterparts (BNHCSs) were synthesized and small Pt nanoparticles deposited on both the inside and outside shell of these materials forming the Pt/BHCSs and Pt/BNHCSs. These materials possess defects that enable good dispersion of metal catalysts. Further, N doping provides anchoring sites for the adsorption of platinum ions and this controls the nucleation and growth of Pt particles which results in the formation of smaller particles with better dispersion [16]. The metal-support interactions of the Pt with the N doped supports thus promote better activity and also durability [17]. The relatively small diameter of the BHCSs ($d < 60$ nm) should allow for better support-support contact between adjacent BHCSs or BNHCSs resulting in good surface area per volume ratios. These smaller supports are also expected to pack more closely compared to bigger spherical supports such as hollow carbon spheres, resulting in better contact between adjacent supports promoting better electronic conductivity. The thin and hemispherical morphology can also promote the deposition of metal nanoparticles on both the inside cavity and on the outer surface resulting in better dispersion of Pt and subsequently better Pt utilization in ORR catalysis.

The new Pt containing materials described in this study were characterized and tested for ORR activity and durability. These catalysts have shown improved MA, SA and catalyst durability as benchmarked against a commercial Pt/C catalyst with a nominal 40 wt.% Pt/C loading. In this study the properties of the supports on which Pt nanoparticles were deposited were varied and the effect of support properties on ORR activity and durability were investigated.

2.Experimental

2.1 Chemicals

Platinum acetylacetonate ($Pt(acac)_2$, 97%), tetraethyl orthosilicate (TEOS, 98%), resorcinol, formaldehyde (37%), hydrofluoric acid (48%), cetyltrimethylammonium bromide (CTAB), melamine (99%), methanol (99%), sulfuric acid (98%) and nafion perfluorinated resin solution (5 wt% in water) were all purchased from Sigma-Aldrich and used as received. Nochromix crystals (Gordax laboratories), ammonia solution (25%, Associated Chemical Enterprises), absolute ethanol (99.6%, MK chemicals), perchloric acid (70%, Suprapur, Merck), ultrapure

water (18.2 MΩ.cm, Merk-Millipore), alumina polish (0.05µm and 0.1 µm and polishing cloths, Buehler), argon gas (99.99%), oxygen gas (99.99%), nitrogen gas (99.99%), were sourced from Afrox and also used as received without further purification.

2.2 Synthesis of small silica templates

Silica particles were prepared according to the method described by Stober and colleagues [18]. To synthesize the small silica particles used as templates for the synthesis of the carbon, absolute ethanol (300 mL) was mixed with tetraethyl orthosilicate (50 mL) and deionized water (50 mL) and allowed to stir at room temperature on a magnetic stirrer for 30 minutes. To this mixture was added 30 mL ammonia solution (25 %) and the reaction was allowed to stir for a further 6 h. Meanwhile, the reaction vessel was sealed to prevent the room temperature evaporation of the ammonia solution. The solution changed from an off-white to a deep white color as the yield of silica increased. The silica particles were separated from solution by centrifugation at 18 000 rpm for a total of 30 minutes. The separated white product was washed with 200 mL of a 50:50 vol % absolute ethanol: deionized water solution and followed by a further centrifugation. The silica was further washed with 100 mL of deionized water and separated by centrifugation and allowed to dry in an oven at 100°C overnight. The silica was placed in a ceramic crucible and calcined at 500°C in air in a muffle furnace for 5 h. The weighed silica powders (18.5 g) amounted to a yield of 88% based on the TEOS used.

2.3 Synthesis of small broken bowl-like hollow carbon spheres (BHCSs)

Typically, a solution of EtOH (280 mL) and DI water (60 mL) was mixed with the SiO_2 spheres (4 g) by sonication. To the solution, a previously sonicated mixture of CTAB (2 g), 37% formaldehyde solution (1.5 mL) and resorcinol (1.5 g) were added. A 25% NH_4OH solution (10 mL) was added and the system was magnetically stirred at room temperature. The solution turned from an off-white color to brown with stirring. After 24 h the SiO_2@RF (resorcinol formaldehyde resin covering the silica) was filtered and washed with copious amounts of DI water, followed by drying in an oven overnight at 100 °C.

The dried brown product was carbonized in a tubular horizontal furnace under an argon flow at 900 °C. Typically, the SiO_2@RF (200 mg) was loaded into a quartz boat and placed in the furnace connected to an argon gas line flowing at 50 mL min^{-1}. The furnace was ramped up to 900 °C at a heating rate of 10 °C min^{-1} and kept isothermal for 2 h followed by a natural cooling

process overnight. The black soot (SiO_2@C) was etched using a 10% HF solution in water (200 ml) for 24 h to remove the SiO_2 template. The solution was vacuum filtered, washed with 500 mL of DI water and dried in an oven at 80 ℃ overnight. The formed BHCSs were annealed in a tubular horizontal furnace at 900 ℃ for 2 h at a heating rate of 10 ℃ min^{-1} under argon flowing at a rate of 50 mL min^{-1}. The weighed BHCSs (250 mg) amounted to a yield of 94% based on the amount of resorcinol used [19].

2.4 Synthesis of nitrogen doped BHCSs (BNHCSs)

Typically, 3 g of SiO_2@RF was mixed with 3 g of melamine in a borosilicate vial containing methanol (20 ml). The composite was sonicated for 30 minutes followed by drying in an oven at 80 ℃ for 2 h. The SiO_2@RF@melamine composite was carbonized at 900 ℃ for 2 h using a heating rate of 10 ℃ min^{-1} under argon, followed by etching to remove the silica with a 10% HF solution (200 mL) for 24 h. The product was filtered and washed with DI water (500 mL) followed by drying at 80℃ in an oven overnight. The BNHCSs were annealed at 900 ℃ for 2 h at a heating rate of 10 ℃ min^{-1} under argon flowing at a rate of 50 ml min^{-1}. The weighed BNHCSs (265 mg) amounted to a yield of 92 % based on the amount of resorcinol used [19].

2.5 Synthesis of Pt/BHCSs and Pt/BNHCSs.

To achieve a nominal 40wt.% Pt/BHCSs or Pt/BNHCSs catalysts, BHCSs or BNHCSs (100 mg) were mixed with $Pt(acac)_2$ (135 mg) and sonicated for 10 min to allow for thorough mixing. The composite was then transferred into a steel cylindrical reactor which was placed in a tubular horizontal furnace under a steady argon stream at 50 mL min^{-1}. The furnace was ramped to 100 ℃ and kept isothermal for 30 min to drive moisture off the sample. The furnace was further ramped up to 350 ℃ at a heating rate of 2.5 ℃ min^{-1} and kept isothermal for 2 h while the reaction continued. The reactor was allowed to cool naturally to room temperature, and the products weighed [20].

2.6 Catalyst characterization

TEM analysis was performed using a Tecnai F20 transmission electron microscope with a field emission gun (FEG) operating at 200 kV. Spatula tips of samples were dispersed in ethanol by ultrasonication and a few droplets were transferred to lacy carbon coated copper grids for TEM analysis. Particle size analysis was carried out by measuring the diameter of at least 100 particles from different TEM images and using the software ImageJ. The particle size distribution was plotted using Origin lab version 8.5. SEM analysis and performed on a Tescan

MIRA3 RISE scanning electron microscope operating at 30kV. Spatula tips of samples were spread on a carbon tape mounted on an aluminium stub and coated with a gold-palladium layer before the analysis to enhance sample conductivity and to reduce charging effects. PXRD measurements were carried out on a Bruker D8 Advance diffractometer with a Cu Kα radiation source operating at 40 kV to determine the crystalline phases present in the catalyst with 2Θ between 0° and 120°. Rietveld refinement of the PXRD patterns was completed using Bruker AXS TOPAS software, Version 4.1. The Scherrer equation was also used to deduce the sizes of the Pt particles. In-situ PXRD experiments were performed under nitrogen on a Bruker D8 Advance diffractometer fitted with an Anton Paar XRK 900 in situ cell. The diffractometer used a sealed copper tube as the X-ray source operating at 40 kV and 40 mA that provided X-rays with a wavelength of 0.15418 nm in a parallel beam geometry. The Rietveld refinement method was used to analyse the PXRD profiles. Indexing the compounds detected by the PXRD technique was achieved using the EVA software. TGA was performed with a Perkin-Elmer STA6000 analyser using N_2 as the purge and coolant gas (20 mL.min^{-1}) and air for combustion (10 mL min^{-1}) and a heating rate of 10 °C min^{-1}. Small amounts of sample (10 mg) were used for TGA analyses. Nitrogen physisorption experiments were conducted using a Micromeritics Tristar 3000 surface area and porosity analyser set at -195 ºC, with sample degassing conducted at 150 °C overnight. The BET surface area was obtained from adsorption data in a relative pressure range from 0.05 to 0.30. The total pore volumes were calculated from the amount of nitrogen gas adsorbed at a relative pressure of 0.99. The pore size distributions were evaluated from the desorption branches of the isotherms using the Barrett-Joyner-Halenda (BJH) method. The micropore surface area and volume were calculated using t-plot data. Raman spectroscopy measurements were performed on a Horiba Jobin-Yvon Raman spectrometer with a laser wavelength of (λ = 514 nm). The XPS measurements were carried out at the National Institute of Meteorology South Africa (NMISA) at the Council for Scientific and Industrial Research (CSIR) in Pretoria, using a Thermo Scientific ESCALAB 250Xi spectrometer with a Monochromatic Al kα (1486.7eV) source operating with an X-ray power of 300 W, X-ray spot size of 900 µm, low resolution pass energy of 100eV, high resolution pass energy of 20 eV and a pressure of 10^{-8} mBar. The catalysts were also studied using scanning transmission electron microscopy (STEM) in a probe corrected JEOL ARM200F at the David Cockayne Centre for Electron Microscopy, University of Oxford, operated at 200 kV. A probe current of 13 pA, convergence semi-angle of 14 mrad, annular dark field (ADF) inner and outer detector angles of 77.43–241.21 mrad, and a bright-field (BF) outer detector angle of 13.2 mrad were used for simultaneous acquisition of both ADF and BF signals.

2.7 Electrochemical characterization

All experiments were performed in a three-electrode cell at room temperature (approx. 25 ºC) in a solution of 0.1 M $HClO_4$. The perchloric acid electrolyte was in all cases saturated with either argon or oxygen for the cyclic voltammetry (CV) or oxygen reduction reaction (ORR) experiments, respectively. A high surface area Pt wire was used as the counter electrode, a $Hg/HgSO_4$ electrode with a bridge tube as a reference electrode and a catalyst coated glassy carbon (GCE) electrode with a working area of 0.196 cm^2 as the working electrode (WE). The reference electrode was calibrated against the reversible hydrogen electrode by measuring the potential difference between the Pt wire in a hydrogen saturated electrolyte. All potentials in these studies were reported against the reversible hydrogen electrode potential (vs. RHE). Catalyst inks were prepared by mixing about 5 mg of the catalyst with 1.5 mL of ultrapure water (18.2 MΩ cm), 3.5 ml isopropyl alcohol (HPLC grade) and 20 µL Nafion per fluorinated resin solution (5 wt % in a mixture of lower aliphatic alcohols and water). The ink mixture was ultra-sonicated in a cold-water bath for 30 minutes to obtain a homogeneous ink solution before analysis. The resulting black ink (10 µL) was pipetted onto the GC electrode (Pine Research Instrumentation or Metrohm-Autolab) coupled to an RDE710 (Gamry) or RDE-2 (Metrohm-Autolab) rotator box and dried under rotation (250 rpm) for 20 minutes in ambient conditions. This formed a thin film of uniformly distributed catalyst on the GC electrode. The ultrapure water and isopropyl alcohol were evaporated during the rotational drying process. The electrochemical cell, electrolyte volumetric flasks, purge tubes and reference electrode bridge tubes were all soaked overnight in a solution of Nochromix and concentrated sulfuric acid. This was followed by a 7 times rinse in ultra-pure water. The GC electrodes were prepared before ink deposition and drying, first using 1 µm alumina and a wet micro-smooth polishing cloth pad. A figure eight cleaning protocol was adopted followed by rinsing in ultra-pure water and ultra-sonication in isopropyl alcohol and ultra-pure water. The routine was repeated with a smoother 0.05 µm alumina polish followed by thorough rinsing to remove the dirt and the sticking alumina. A Biologic SP300 potentiostat or Metrohm Autolab PGSTAT302N coupled to a Gamry RDE (rotating disk electrode) 710 Rotator or a Autolab RDE-2 rotator was used for CV and RDE measurements.

In an Ar saturated electrolyte, the potential of the WE was cycled between 0.0 and 1.2 V vs. RHE for 100 cycles at 100 mV s^{-1} for the electrochemical oxidation of all the impurities on the surface of the catalyst coated WE. The scan rate was then reduced to 50 mV. s^{-1} and the 3rd cycle was used for the calculation of the electrochemical active surface area (ECSA) assuming

a monolayer charge associated with hydrogen adsorption of 210 µC cm^{-2} [21]. The area under the CV curve, associated with the under potential deposition of hydrogen, was integrated and used for the calculation of ECSA. Oxygen reduction reaction (ORR) I-V polarization curves were obtained at 1600 rpm of the electro-catalyst coated working electrode. The WE was cycled at 10 mV s^{-1} between 0.0 – 1.2 V vs. RHE in the cathodic direction. To correct for non-ORR background current, the LSV obtained in an argon saturated electrolyte without rotation was subtracted from that obtained from the oxygen saturated electrolyte. The kinetic ORR currents (I_k) were extracted from the measured ORR currents (I) and the limiting currents (I_{lim}) determined at 0.4 V vs. RHE using the Koutecky-Levich equation. Finally, kinetic currents were normalised with the ECSA and the initial Pt mass loading to obtain the surface area specific activity (SA) and the mass-specific activity (MA), respectively. All the activity data reported was obtained with cathodic scans and not corrected for mass transport and solution resistance.

Durability load cycling was carried out after the measurement of the beginning of life (BOL) CV and ORR activity [22]. Initially the WE was cycled between 0.0 – 1.2 V vs. RHE at 100 mV s^{-1} to clean the catalysts of any impurities and contaminants and to produce a reproducible CV. This was followed by 3 CVs at a lower scan rate of 20 mV s^{-1} for ECSA measurements. At the end of each load cycling CV set, three CVs were obtained, and the 3rd was used for the calculation of the new ECSA. Load cycling for catalyst durability measurements was carried out in a 0.1 M $HClO_4$ solution at 25 ºC, in an argon saturated solution. The WE was cycled at 50 mV s^{-1} between 0.6 – 1.0 V vs. RHE using a triangular wave profile with zero seconds hold at each potential and a complete cycle duration of 16 seconds (Figure S12 and Figure S13) [23]. Load cycling was carried out in units of 10, 100, and 1000 cycles until when the 6000th cycle was reached after 27 h of continuous cycling and argon saturation. As Pt durability was under investigation, in all durability experiments, the Pt counter electrode was replaced with a gold counter electrode of high surface area.

3. Results and Discussion

3.1 Synthesis and characterization of BHCSs and BNHCSs

The synthesis of the silica templates followed standard procedures [18]. However, conditions were chosen to make small silica spheres (d *ca.* 60 nm; Figure S1)). The SiO_2 spheres were then reacted with formaldehyde and resorcinol mixture, together with CTAB (to produce a porous structure) under hydrothermal conditions to produce SiO_2@RF. Removal of the silica

produced the bowl-like broken hollow carbon spheres (BHCSs) (Figure S2). Reaction of SiO_2@RF with melamine, a nitrogen source, produced SiO_2@RF@Melamine and after thermal reaction and removal of the silica, the nitrogen covered BHCSs (BNHCSs) were produced (Figure S2) A schematic showing the synthesis procedure is shown in Figure 1.

The broken bowl-like morphologies of the BHCSs and the BNHCSs were indicated in the SEM and TEM images [24]. The hemispheres interact with each other with no observable morphological changes in the SEM images of the materials after nitrogen doping. This indicates that the solid melamine used for the doping process infused into the structure of the BHCSs altering only the chemical composition but not the morphology of the material. The materials had thin shells of d = 4.5 ± 0.6 nm and d = 4.6 ± 0.9 nm and external diameters of 58 ± 0.9 nm and 60 ±1.1 nm for the BHCSs and BNHCSs, respectively (Figure S3). The similarity in support diameter and shell thickness for both materials also indicates that the nitrogen doping process did not significantly contribute to an increase in shell thickness or diameter of the materials.

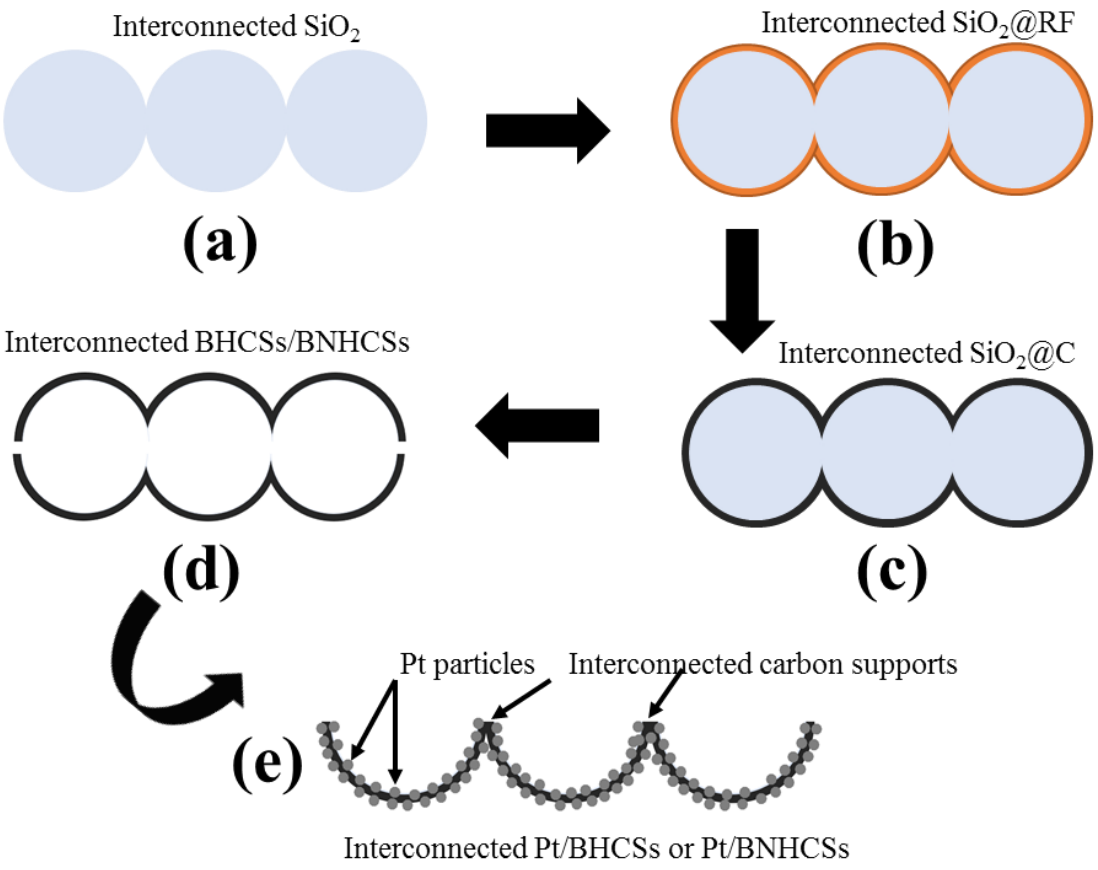

Figure 1: Schematic of the formation of Pt/BHCSs and Pt/BNHCSs. (a) interconnected SiO_2, (b) interconnected SiO_2@RF, (c) interconnected SiO_2@C, (d) interconnected BHCSs or BNHCSs and (e) interconnected Pt/BHCSs or Pt/BNHCSs

The BHCSs and BNHCSs were characterized using Raman spectroscopy to determine the structural order and defects in the material. Deconvolution of the area under the Raman spectra (Figure S4) was used to separate the contributions of the respective D, D1, D2 and G bands. The G band of the materials is due to the contributions of the vibrational modes of graphite like sp^2 hybridized carbon [25] while the D band contribution is due to defective sp^3 hybridized carbon. The ratio of the contributions of the D and the G band areas (I_D/I_G) is a measure of the extent of graphitization and defects in the materials. The BHCSs had an I_D/I_G of 0.97 while the BNHCSs had an I_D/I_G of 1.00 (Table S1). The marginally higher I_D/I_G for the BNHCSs was expected as nitrogen doping causes an increase of the number of defects in the structure of the carbon [26]. The extent of graphitization of the materials was also measured by the position of the G band which occurs at lower frequency for highly graphitic materials and at higher frequency for the less graphitic or amorphous materials, as suggested by Ferrari and co-workers [27]. The G band of the BHCSs occurred at 1586 cm^{-1} while the BNHCSs had a G band at 1595

cm^{-1} (Table 1) indicating that the BHCSs are more graphitic. The G band shift is also shown in the overlaid deconvoluted Raman spectra (Figure S1).

The BHCSs and BNHCSs were analysed using TGA (up to 900ºC) in air to investigate the thermal stability of the materials under oxidizing conditions. The TGA and DTGA (differential TGA) profiles of the BHCSs and BNHCSs are reported in Figure S5. The pristine BHCSs were found to have a higher decomposition temperature of 780ºC compared to 680ºC for the N doped carbon. The lower decomposition temperature for the doped BNHCSs is attributed to the higher defect density due to N doping which makes the C less thermally stable than the more ordered and graphitic BHCSs [19]. For both materials, the final residual weight (%) is zero which indicates that at 900ºC all the C has decomposed. This is also an indication that the SiO_2 etching process was successful and the materials did not contain SiO_2 impurities

3.2 Synthesis and characterization of the Pt/BHCSs and Pt/BNHCSs

The BHCSs or BNHCSs supports were reacted with $Pt(acac)_2$ to give Pt/BHCSs or Pt/BNHCSs catalysts with a nominal weight loading of 40wt.%. This was achieved in a tubular horizontal at 350 ℃ [20]

The synthesized Pt nanoparticles appear to have a quasi-spherical morphology (Figure 2) with measured particle sizes of 3.9 ± 0.5 nm and 3.8 ± 0.6 nm (Table 1) for the Pt/BHCSs and Pt/BNHCSs respectively (Table 1).

A strong support interaction is suggested by the small inter-particle distances of the Pt nanoparticles deposited on both supports (6.5 ± 0.5 nm for Pt/BHCSs and 6.4 ± 0.2 nm for Pt/BNHCSs (Figure S6, Table 1)). The smaller Pt interparticle distances are due to the metal organic deposition technique used and the numerous defects on the supports that provides numerous nucleation sites for Pt during deposition [28]. The Pt nanoparticles supported on BNHCSs were expected to have smaller inter-particle distance due to the combination of electron rich nitrogen groups and defects that improved the nucleation and growth dynamics of the Pt particles [29].

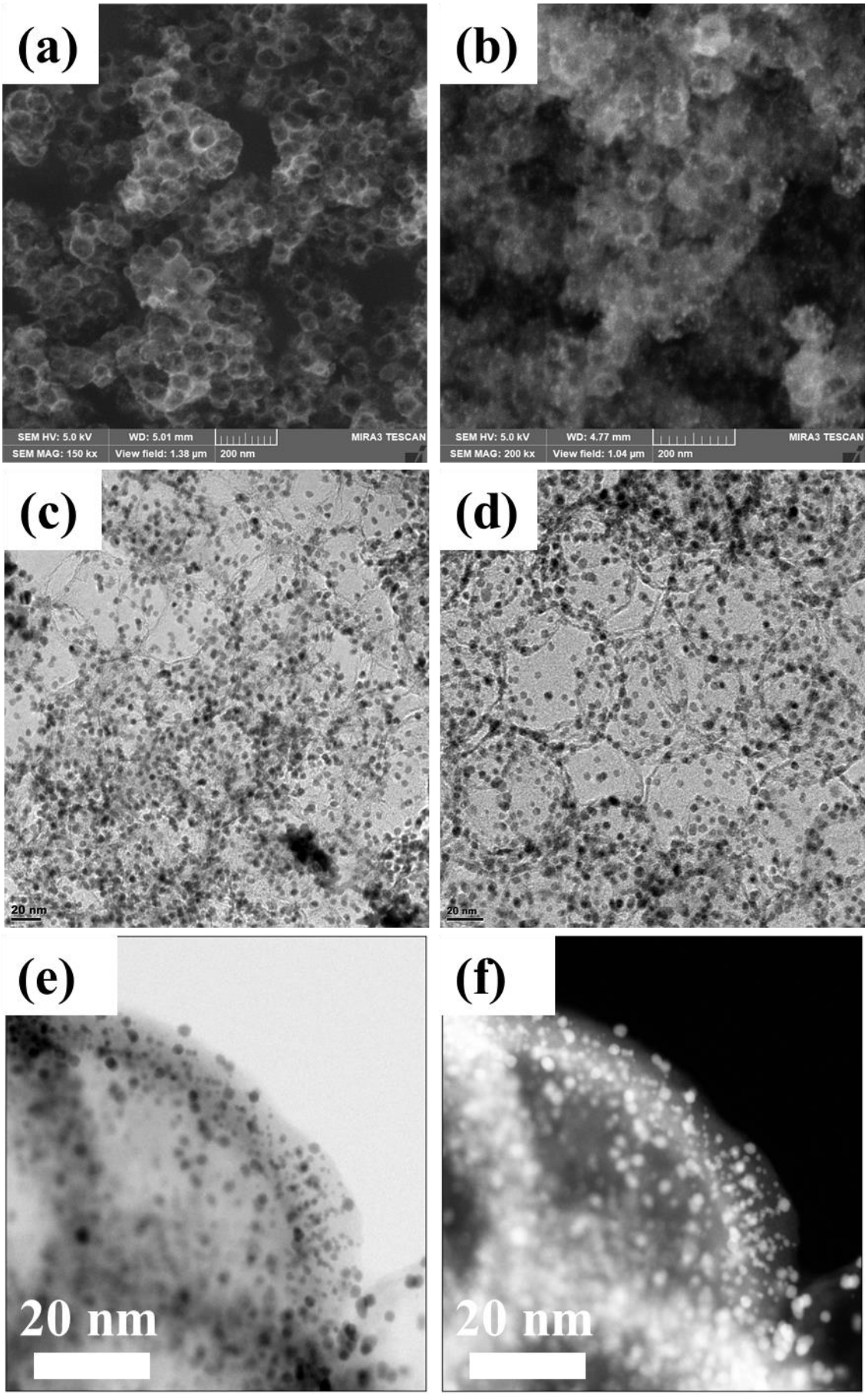
(a)
SEM HV: 5.0 kV
WD: 5.01 mm
MIRA3 TESCAN
SEM MAG: 150 kx
View field: 1.38 μm
200 nm
(b)
SEM HV: 5.0 kV
WD: 4.77 mm
MIRA3 TESCAN
SEM MAG: 200 kx
View field: 1.04 μm
200 nm
(c)
20 nm
(d)
20 nm
(e)
20 nm
(f)
20 nm

Figure 2: SEM images of (a) Pt/BHCSs, (b) Pt/BNHCSs. TEM images of (c) Pt/BHCSs, (d) Pt/BNHCSs, STEM BF-ADF images of (e-f) Pt/BNHCSs

Using STEM BF-ADF (Figure 2(e-f)), it was shown that the Pt nanoparticles are mostly embedded within the shell of the support. This is reflected by the brighter ADF contrast in the shells compared to the hollow interior of the BHCSs and BNHCSs supports, and the lack of Pt nanoparticles protruding into the vacuum at the support surface. This embedding of Pt nanoparticles in the support pores and voids is known as pore confinement [30-33]. Pt confined inside the pores and the voids of the support will be strongly bound and more resistant to degradation due to detachment, dissolution and agglomeration. The local atomic structure of the Pt/BHCSs and Pt/BNHCSs was investigated using aberration-corrected STEM BF-ADF imaging (Figure 3 (a -d)). Here, the two catalysts showed no differences in the crystallographic phase of the Pt nanoparticles at the local scale, consistent with the phase determined by bulk PXRD, discussed later. The high-resolution STEM BF-ADF images (Figure 3 (a-d)) showed hexagonal faceted Pt nanoparticles. Examination of the power spectrum (Figure 3 (b) insert) and the measured 0.24 nm interplanar spacing consistent with {111} planes is consistent with a typical <110> face-centred cubic (fcc) structure that is characteristic of Pt particles enclosed with {111} facets (Figure 3 (a)). Some of the Pt nanoparticles (Figure 3 (a-d)) exhibit twin boundary defects commonly observed in fcc transition metals due to symmetrically mirrored <111> fcc Pt grains [34]. According to DFT studies [35], {111} surfaces in fcc Pt are considered to be the active sites for ORR, however in contrast to flat facets, twin boundaries are essential defects in catalysis since they typically have higher adsorption energies in comparison to flat facets and are stable during chemical reactions [36].

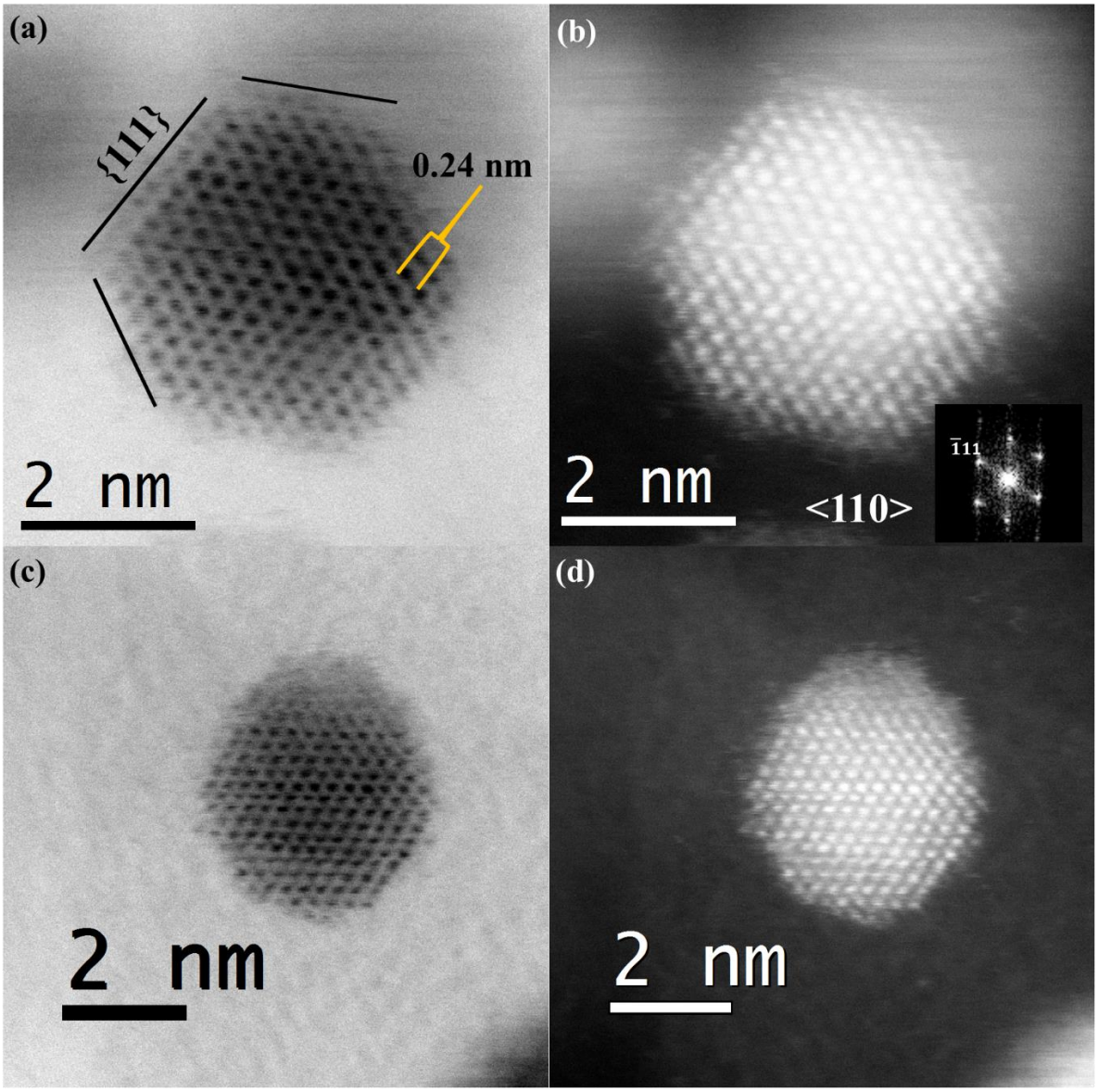

Figure 3: High resolution BF-ADF STEM images of (a-b) Pt/BHCSs and (c-d) Pt/BNHCSs. The insert in (b) is the power spectrum of a <110> projection of fcc Pt

The textual properties and surface area of the materials were investigated using BET and BJH methods. The materials were both found to exhibit a combination of type II and type IV BET isotherms (Figure 4) that is characterized by monolayer gas physisorption at low relative pressure and multilayer gas adsorption at high relative pressure [37]. The isotherms show a significant change in the size of the hysteresis loop of the Pt/BHCSs and Pt/BNHCSs compared to the supports. The smaller hysteresis loop for the Pt supported catalysts indicate that there is less capillary condensation of the inert gas for the Pt/BHCSs and Pt/BNHCSs compared to the supports due to the reduced size of pores, as a result of Pt confinement.

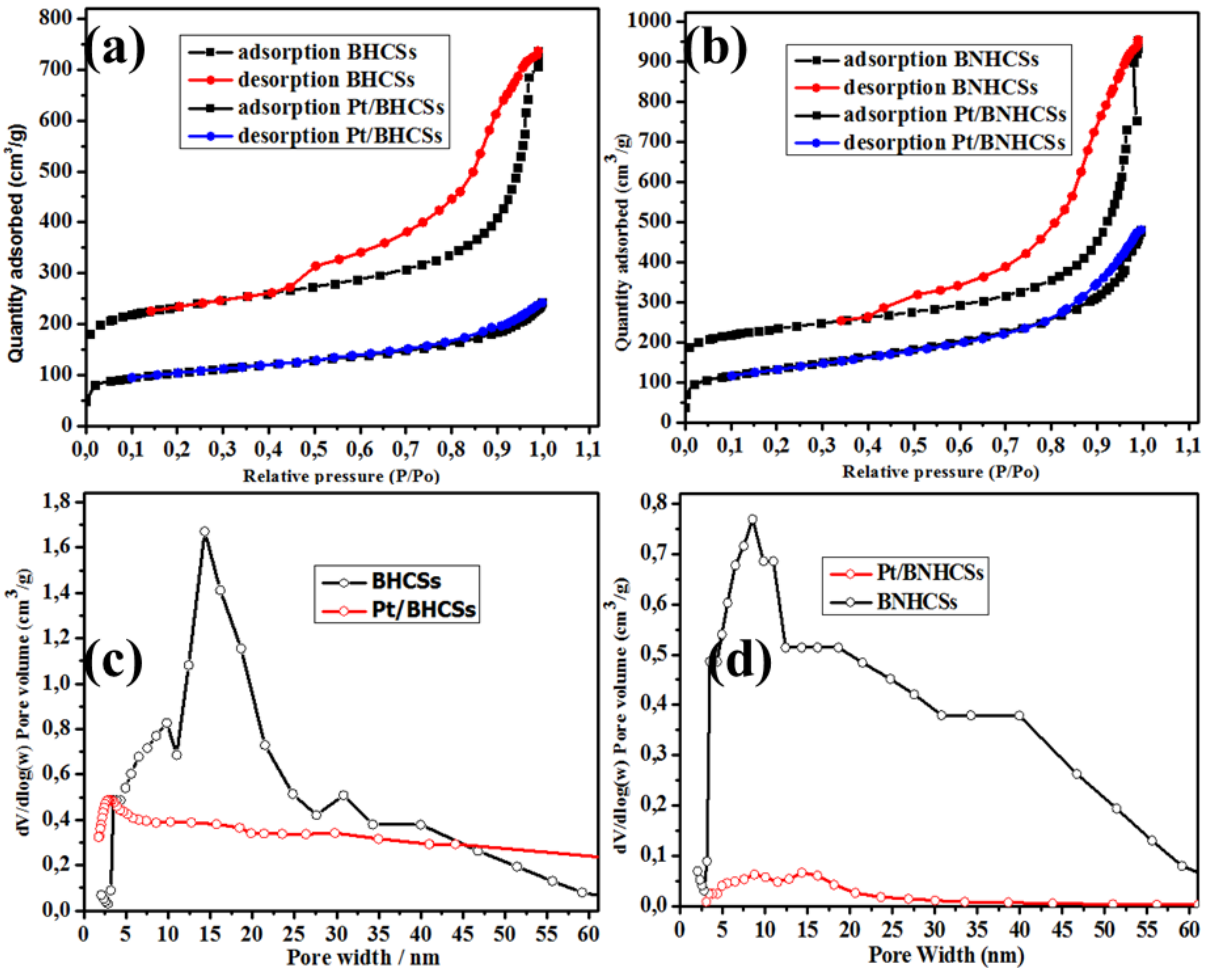

Figure 4: BET isotherms for (a) BHCSs and Pt/BHCSs, (b) BNHCSs and Pt/BNHCSs. Pore size distribution plots for (c) BHCSs and Pt/BHCSs and (d) BNHCSs and Pt/BNHCSs.

The pristine BHCSs and the BNHCSs had comparably high BET surface areas of 755 m^2 g^{-1} and 782 m^2 g^{-1} (Table S2), respectively. After deposition of the Pt nanoparticles the Pt/BHCSs had a BET surface area of 461 m^2 g^{-1} while the Pt/BNHCSs, had a surface area of 347 m^2 g^{-1}. This reduction in surface area is coupled with a 43 % reduction in pore volume for the BHCSs sample. For the BNHCSs and Pt/BNHCSs, there is an observed 80 % reduction in pore volume (Table S2). There is also an observable change in the pore structure of the Pt supported materials versus the pristine and the nitrogen doped supports. The pores with significant volume are widely distributed between 5 and 30 nm for both supports (Figure 4). However, after the deposition of platinum the pores with significant volume were now mostly in the 2 to 10 nm range for the BHCSs and Pt/BHCSs samples. For the BNHCSs and Pt/BNHCSs samples, pores with significant volume changed from 5 to 60 nm to 2 to 20 nm respectively.

The reduction in textual properties due to the deposition of platinum was attributed to some of the Pt nanoparticles being confined inside the pores of the supports, hence changing the overall pore structure of the metal supported materials [38]. This is consistent with the particle sizes and TEM/SEM analysis discussed above. In summary, some of the Pt nanoparticles deposited blocked the pores of the supports, either fully or partially, resulting in a reduction of the overall pore sizes.

Importantly, since the Pt particle (ca. 4 nm) is almost as wide as the carbon thickness of the BHCS and BNHCS supports this suggests that a single Pt particle will be available for catalytic reactions on both sides of a pore (see below). Further, while the single Pt particle is exposed on both side of the carbon sheet it will also have strong Pt-C or Pt-NC support interactions when it resides in a pore.

The TGA and DTGA profiles of Pt/BHCSs and Pt/BNHCSs are shown in Figure S6. The residual Pt was found to be 40.5 wt % for both the Pt/BHCSs and Pt/BNHCSs catalysts. The deposition of Pt nanoparticles enhanced the combustion of the C and consequently lowered the thermal stability of the materials as shown by the lower decomposition temperatures of the Pt/BHCSs. The decomposition of Pt/BNHCSs also occurred at a lower temperature compared to the BNHCSs. This catalytic effect of Pt enables the faster combustion of the C supports and hence enables the process to occur at lower temperatures than for the support materials [39]. The Pt/BHCSs and Pt/BNHCSs showed multiple decomposition temperatures corresponding to disordered and ordered C for the low and high decomposition temperatures, respectively [40].

The crystallinity of the materials was investigated using PXRD and the corresponding diffractograms were also used to estimate the Pt particle size using Rietveld refinement and the Scherrer equation. Both the BHCSs and BNHCSs showed a structure typical of turbostratic C made mostly of amorphous carbons characterized by PXRD peak broadness (Figure 5 a). The Pt on the BHCSs and BNHCSs showed reflections characteristic of the fcc unit cell of Pt [41] (Figure 5b), in agreement with the ADF-BF STEM studies (Figure 3). Rietveld refinement of the Pt peaks yielded a Pt crystallite size of 5.2 ± 1.2 nm (Pt/BHCSs) and 4.8 ± 0.9 nm (Pt/BNHCSs) (Table 1). The Pt crystallite sizes as determined using the Scherrer equation were 4.5 ± 0.7 nm and 4.3 ± 0.8 nm for Pt/BHCSs and Pt/BNHCSs respectively. As expected, the Pt nanoparticles are smaller in the nitrogen doped support [42] and the particle diameters measured using PXRD are comparable to the TEM particle diameters.

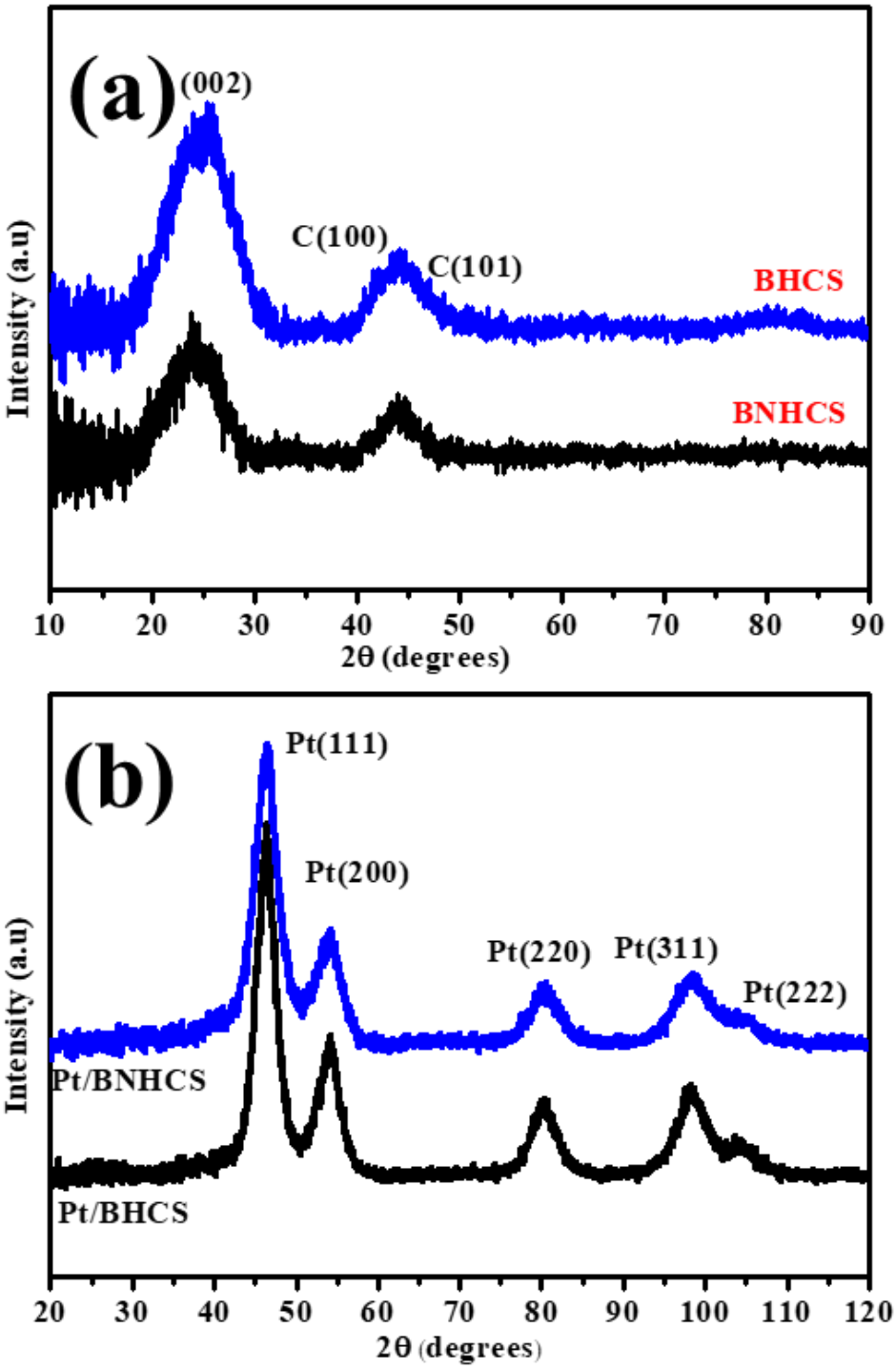

Figure 5: PXRD diffractograms of (a) BHCSs and BNHCSs, (b) Pt/BHCSs and Pt/BNHCSs

The Pt nanoparticle sizes were slightly bigger than the TEM measured nanoparticles as expected from the volume averaging of particle sizes, as done in PXRD measurement of

crystallite size, which tend to overlook the smaller crystallites over the larger ones [43]. Further, the reported particle sizes follow a similar trend as found for the BNHCSs with smaller nanoparticles than the BHCSs.

Table 1: Pt crystallite sizes of Pt/BHCSs, Pt/BNHCSs and the commercial benchmark Pt/C as measured by TEM, the Scherrer equation and Rietveld refinement

Size/nm	Pt/BHCSs	Pt/BNHCSs	Pt/C
TEM	3.9 ± 0.5	3.8 ± 0.6	3.9 ± 0.9
Scherrer	4.5 ± 0.8	4.3 ± 0.8	4.1 ± 1.2
Rietveld	5.2 ± 1.2	4.8 ± 0.9	4.7 ± 0.6
Pt-Pt distance/nm	6.5 ± 0.5	6.4 ± 0.2	6.7 ± 0.8

To investigate Pt pore confinement and its influence on durability, the catalysts were heated from 25 – 725 ℃ in in-situ PXRD measurements (Figure S7). Ideally, without pore confinement, heating of the Pt should cause substantial Pt crystallite growth. However, the Pt crystallite size increased from 5.2 nm (Rietveld refinement) at 25 ℃ to 5.3 nm at 725 ℃, which corresponds to a 3 % change in the Pt crystallite size for the Pt/BNHCSs catalyst. Correspondingly crystallite size growth of 15 % and 38 % were observed for the Pt/BHCSs sample and the commercial Pt/C respectively (Figure S8 and S9). The improved tethering reduced the agglomeration and dissolution of the Pt due to strong bonding that with the supports for the Pt/BHCSs and Pt/BNHCSs samples. We also note the comparable pore sizes for the supports and the size of the resulting Pt nanoparticles. The Pt nanoparticles (3.9 nm on average) and the average pore widths for Pt/BHCSs (6.8 nm) and Pt/BNHCS (5.5 nm) (Table 1 and Table S2) respectively have resulted in Pt nanoparticles that can fit into the pores leading to improved contact with the supports. Nitrogen doping of the BNHCSs could also have promoted better contact or tethering between the Pt and the support restricting crystallite growth due to

in-situ heating [44]. Meanwhile, the low BET surface area and pore structure of the commercial Pt/C catalysts could not prevent crystallite growth of the Pt.

XPS was used for the analysis of the chemical bonding of the constituents in the surface regions of the materials of both Pt/BHCSs and Pt/BNHCSs. Low resolution surface surveys were obtained in the 50 – 550 eV binding energy window (Figure S10). To compensate for sample charging effects, the binding energy of adventitious sp^2 C (284.3 eV) was used as a calibration standard [45]. The C1s spectra were deconvoluted into their component peaks (C = C, C – C, C – C, O - C = O and C = O bonds) for both Pt/BHCSs and Pt/BNHCSs (Figures S10 and Figure 6) [46]. Deconvolution of the C species present indicates the presence of ca. 31 at % sp^2 (C = C) hybridized carbon for the Pt/BHCSs compared to 26 at % for the Pt/BNHCSs. The increased graphitic carbon in the Pt/BHCSs indicates the presence of fewer defects in the C of this sample compared to the N doped Pt/BNHCSs. Deconvolution of the O1s spectra (Figures S10 and Figure 6) showed the presence of quinones (530.3 eV), C = O bonds (531.2 eV), C – O bonds (532.0 eV) and terminal O –H bonds (533.1 eV). Deconvolution of the N1s high resolution spectra for Pt/BNHCSs (Figure 6) showed the presence of pyridinic nitrogen (398.3 eV), pyrrolic nitrogen (400.7 eV), graphitic N (401.6 eV), oxidized N (403.1 eV) and metal bonded N (metal-N-pyridyl) nitrogen (399.7 eV) (table 2) [47]. The total atomic % contribution of the N groups were ca. 7.4 at %, an indication that the doping process was successful. The functional groups shown by the deconvolution of the XPS spectra indicated the presence of a chemically active support surface able to influence the behaviour of the Pt catalyst through processes such as charge transfer, better Pt-support contact, and better Pt-support interactions [48]. It is also to be noted that functionalized carbons have shown promising ORR catalysis without the involvement of precious metal catalysts [49].

Table 2: Data for the deconvoluted high resolution N1s spectra for Pt/BNHCSs

Sample	N1s				
	Pyridinic N	Metal Nitrile	Pyrrolic N	Graphitic N	Oxidized N
(BE/eV) Pt/BNHCS	398.3	399.7	400.7	401.6	403.1
(Atomic%) Pt/BNHCS	1.4	1.2	2.1	1.8	0.9

The Pt4f spectra for Pt/BHCSs and Pt/BNHCSs samples were also deconvolved (Figures S10 and Figure 6) with peak assignments are shown in Table 3. Upward Pt binding energy shifts were observed for the Pt/BNHCSs when compared to the Pt/BHCSs (Figure S11).

Table 3: Data for the deconvoluted high resolution Pt 4f spectra for Pt/BHCs and Pt/BNHCSs

	Pt4f			
Sample	Pt 4f7- metal	Pt 4f7 – PtO	Pt4f5 - metal	Pt4f5 – PtO
(BE/eV)Pt/BHCS	71.0	72.0	74.4	75.5
(BE/eV)Pt/BNHCS	70.9	71.7	74.2	75.2
Δ eV	0.1	0.3	0.2	0.3
(Atomic%)Pt/BHCSs	2.0	0.6	2.0	0.6
(Atomic%)Pt/BNHCSs	2.0	0.4	2.0	0.4
Δ Atomic %	0	0.2	0	0.2

The shifts in the binding energies are attributed to different interactions between the Pt and the BHCSs and BNHCSs supports. The Pt 4f spectra were deconvolved into metallic Pt and oxidized Pt (PtO) with metallic Pt accounting for more than 90 at. % of Pt species present in both samples. This shows that most of the Pt on the surface and in the pores of both the catalysts is metallic Pt.

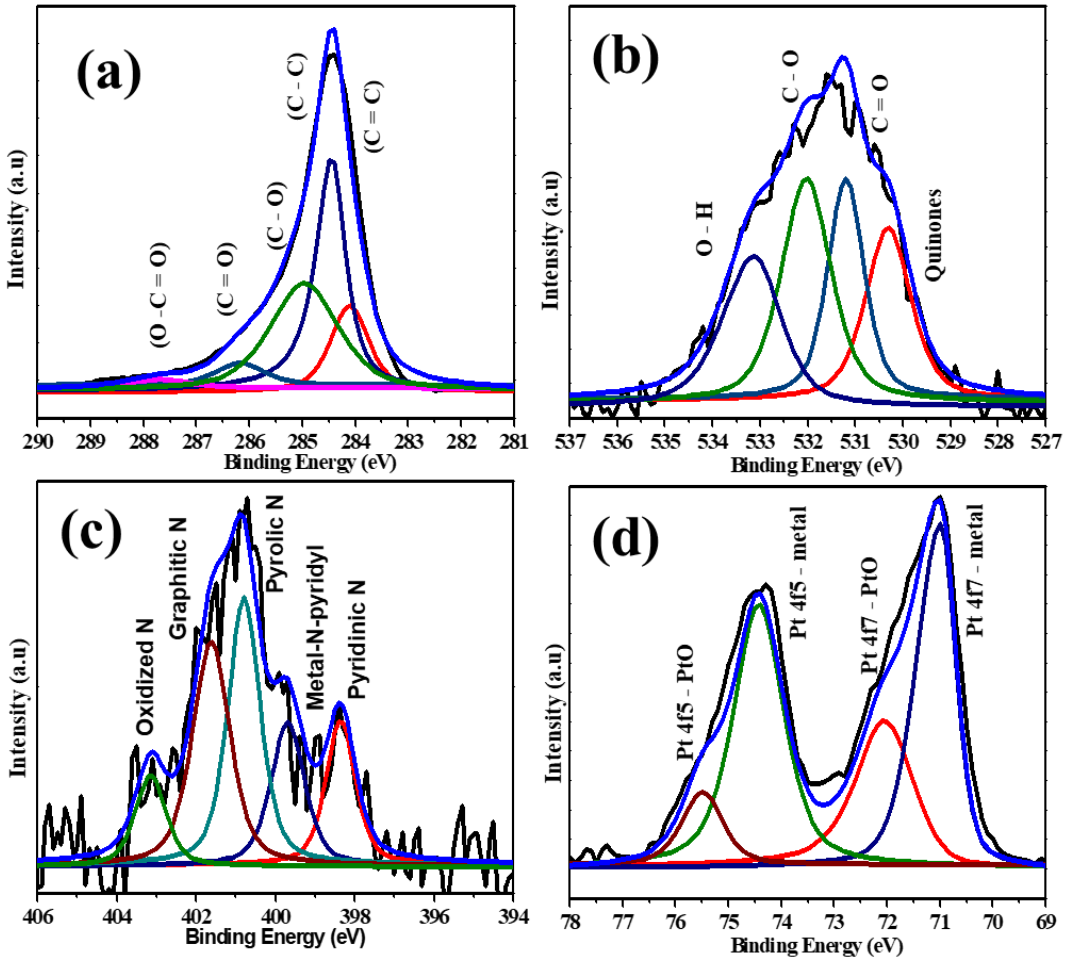

Figure 6: Deconvoluted high resolution XPS spectra for Pt/BNHCSs (a) C1s, (b) O1s, (c) N1s and (d) Pt 4f

3.3. Electrochemical characterization

3.3.1 Catalyst activity

Electrocatalysis characterisation of the catalysts are presented in Figure 7. The materials were studied using cyclic voltammetry and linear sweep voltammetry for ORR activity. All samples exhibited typical features of a Pt/C catalyst (Figure 7a) specifically the peaks for under potential deposition of H_2, $H_{UPD,}$ region, 0.0 – 0.4 V vs. RHE and peaks for the desorption of H_2 in the same potential window in the positive scan direction. For all the catalysts there is no observable peak in the 0.4 - 0.5 V vs RHE region as this is the double layer region of the cyclic voltammogram (CV), due to the capacitive effects of the materials. Pt oxidation occurred as

shown by the peaks between 0.75 - 1.2 V vs RHE. In this region a clean Pt surface was oxidised to PtO and at the reversal of the cycle, in the same region of 1.2 – 0.75 V, the PtO was reduced back to metallic Pt. All the materials have a differently sized capacitive double layer due to the variety in the chemical nature of the different support materials. The respective ECSAs were between 61 – 69 m^2 g^{-1} consistent with the metal surface area calculated from the measured TEM particle sizes (Table S3) [50]. The Pt/BNHCSs catalyst displayed an unusually high ECSA at 69 m^2 g^{-1} for a 3.9 nm average diameter, even though other similar particle sizes for the Pt/BHCSs and commercial benchmark Pt/C had lower ECSA values (Table 4). This, and the observed higher diffusion limiting current in both the Pt/BNHCSs and Pt/BHCSs (Figure 7b) was attributed to the structure of the catalyst, whereby the roughness of the hemispherical small supports in the catalyst film enabled the exposure of more Pt active sites (Figure 1). Unlike the commercial benchmark Pt/C catalyst where the Pt was deposited only on the outside surface of the supports, in these catalyst systems, Pt is deposited both inside and outside the broken shell. Therefore, more Pt active sites were exposed to the oxygen saturated electrolyte for the Pt/BHCSs and Pt/BNHCSs compared to the commercial benchmark Pt/C [51].

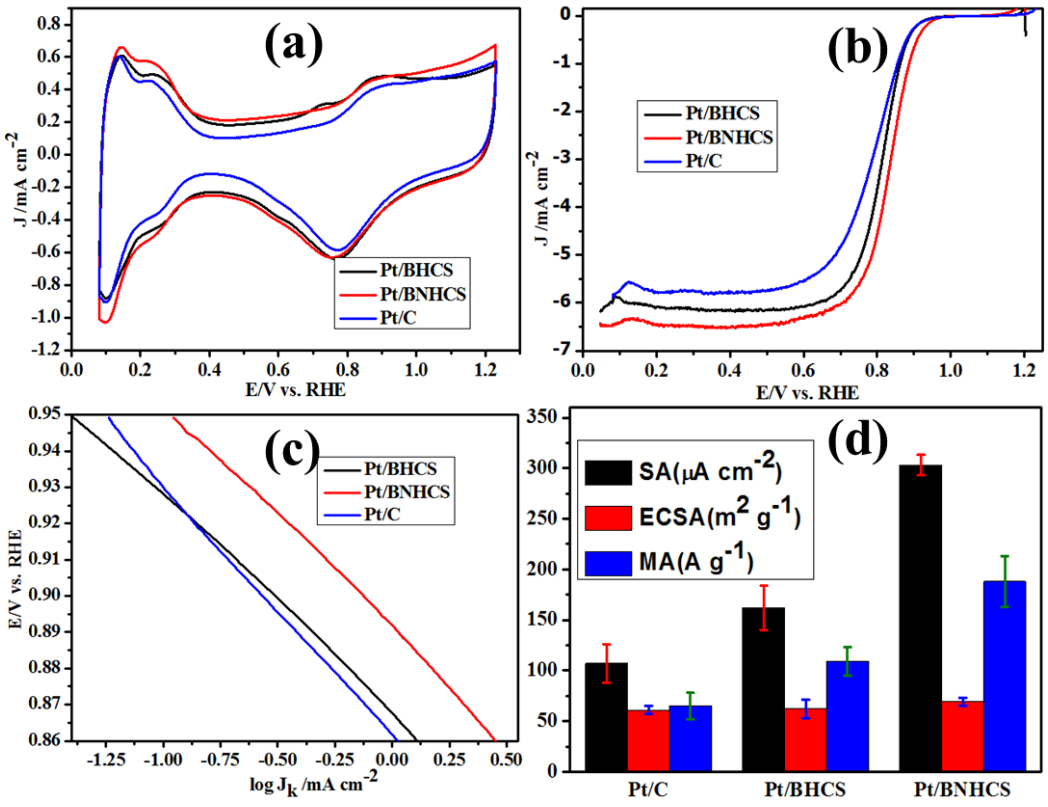

Figure 7: The (a) Cyclic voltammograms, (b) ORR polarization I-V curves, (c) Tafel plots and (d) ORR activity and ECSA data for the Pt/BHCSs, Pt/BNHCSs and the commercial benchmark Pt/C

At an electrode potential of 0.90 V vs. RHE, the kinetic current as provided by the Tafel plots (Figure 7c) show the order of catalyst activity follows the trend Pt /BNHCSs > Pt/BHCSs > commercial benchmark Pt/C (Table 4). The Pt/BHCSs has the highest kinetic current of 3.0 mA cm^{-2} compared to 1.1 mA cm^{-2} for the benchmark Pt/C. This is a 172 % increase in the kinetic current for this material. There is also a small 18 % increase in the kinetic current for the Pt/BHCSs compared to the commercial benchmark Pt/C at 0.90 V vs. RHE.

The kinetic currents were normalised with the ECSA to yield area specific activities (SA) of the catalysts. Both the Pt/BHCSs and Pt/BNHCSs catalysts had higher SA activities compared to the commercial catalyst (Pt/C). The Pt/BNHCSs had a SA that is 183 % larger than the commercial benchmark catalyst (Table 4) whereas the Pt/BHCSs had a SA value that is 51 % larger than that of the benchmark catalyst.

Table 4: Calculated ECSA and ORR activity for the Pt/BHCSs, Pt/BNHCSs and the commercial benchmark Pt/C catalysts. MA, SA, I_k measurements obtained at 0.90 V vs. RHE.

Catalyst	ECSA / (m^2 g^{-1})	MA (0.90V) / (A g^{-1})	SA (0.90V) /(µA cm^{-2})	I_k (0.90V) /(mA cm^{-2})	$E_{1/2}$ V. vs RHE	E_{onset} V. vs RHE
Pt/C	61 ± 4	65 ± 13	107 ± 19	1.1 ± 10	0.787	0.941
Pt/BHCSs	62 ± 9	109 ± 14	162 ± 22	1.3 ± 18	0.804	0.953
Pt/BNHCSs	69 ± 4	188 ± 25	303 ± 10	3.0 ± 30	0.836	0.998

Kinetic currents were normalised with the loading of the catalysts on the WE to yield the mass specific activities (MA). The observed trend is similar to the SA, with Pt/BNHCSs exhibiting a 189 % larger MA (188 A g^{-1}) compared to Pt/C (65 A g^{-1}). There was a 67% increase in MA for the Pt/BHCSs (109 A g^{-1}) relative to the commercial benchmark Pt/C catalyst. Also, of note is the order of the ORR onset potential (Table 4) which is Pt/BNHCs > Pt/BHCSs > Pt/C. The same trend is seen in the half wave ORR potentials for these materials (Table 4), demonstrating that the Pt/BNHCSs is a better ORR catalyst than the Pt/BHCSs and the commercial benchmark Pt/C. The trends in SA and MA of the catalysts are shown in Figure 7d.

The differences in activity (SA and MA) were attributed to the different nature of the supports and the effects introduced by N doping which affected the electronic properties of the catalysts. The BHCSs and BNHCSs supports are also hemispherical, interconnected C supports as

opposed to the C of the commercial benchmark which has a solid core. The BHCSs supports are interconnected with thin shells (Figure S3) and the Pt nanoparticles are deposited on both sides of the shells with smaller Pt- Pt interparticle distances (Table 1). The XPS data (Figure 6, Table 2) confirmed the presence of N1s electronic states for Pt/BNHCSs which were not present in the Pt/C and Pt/BHCSs catalysts and the electronic interactions between the Pt and the N-groups promoted better activity for the doped materials compared to the pristine catalysts [52].

The highly active Pt/BNHCSs and Pt/BHCSs have twice the BET surface area compared to the Pt/C catalyst with a BET surface area of 220 $m^2 g^{-1}$ with higher pore widths for the Pt/BHCSs and Pt/BNHCSs of 6.8 nm and 5.5 nm, respectively compared to 4.8 nm for the Pt/C catalyst. This larger pore size allows the confinement of Pt nanoparticles inside the pores of the supports forming a matrix of Pt/C that in turn promotes metal to support electronic conductivity. The larger pores in the Pt/BHCSs and Pt/BNHCSs facilitates better mass transport and diffusion of the O_2 in the ORR experiments as well as the removal of water from the Pt surface on completion of the ORR reaction.

A comparison with other similar Pt loaded (Pt/C) catalysts has been made (Table 5), and from the results provided, it can be seen that the materials described here exhibit ECSA, mass specific activity and area specific activity comparable to other carbon based supports as well as to other catalysts where confinement of Pt has been reported.

Table 5: Comparison of Pt/BNHCSs and Pt/BHCSs to other Pt/C catalysts reported. MA, and SA data are calculated from data at 0.90 V vs. RHE.

Sample	Pt loading (wt %)	ECSA ($m^2 g^{-1}$)	MA ($A g^{-1}$)	SA (μAcm^{-2})	Comments	Ref
Pt/BNHCSs	40	69 ± 4	188	303	Pt pore confinement	This work
Pt/BHCSs	40	62 ± 9	109	162	Pt pore confinement	This work
Pt/C (HiSpec4000)	38	61 ± 4	65	107	No Pt pore confinement	This work

Pt_{inside}/KJ600	40	113	550	492	Pt Pore confinement	32
Pt@GB-1	28	-	175	-	Pt pore confinement	33
Pt@GB-2	52	-	134	-	Pt pore confinement	33
Pt@HGS	20	75±11	350	470	Pt pore confinement	31

3.4.2: Catalyst Durability

The durability CVs of the catalysts are shown in Figure 8 (b-d). The CV profiles show that for all the catalysts, the intensities of the signals relating to H_2 adsorption and desorption in the 0.0 - 0.4 V vs. RHE region as well as in the Pt - oxide formation and reduction region above 0.5 V vs. RHE decreased as a result of the potential cycling. Two parameters were used for investigating support durability; the changes in the double layer capacitance and the formation of hydroquinone/quinone (HQ/Q) functionalities as C is partially oxidised [53].

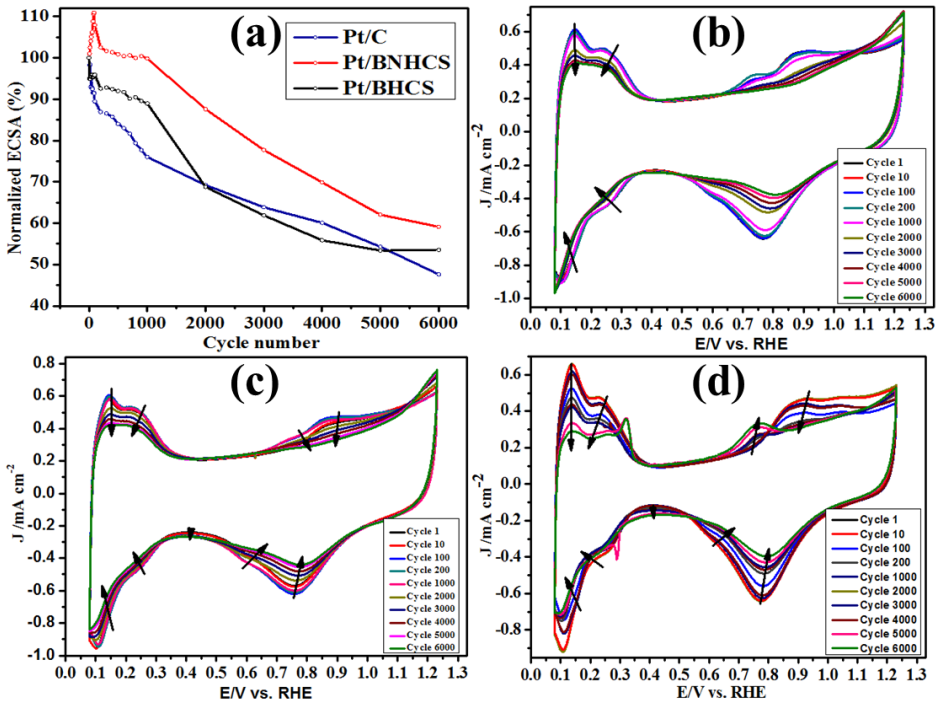

Figure 8: (a) Normalized ECSA% degradation of the catalysts, (b-d) durability CVSs for the Pt/BHCSs, Pt/BNHCSs and the commercial benchmark Pt/C catalysts

Carbon corrosion is usually observed from the CV curves during the oxidation of hydroquinone to quinone and this normally occurs as a redox peak at about 0.6 V vs. RHE. The released charge coupled to partial oxidation in the HQ/Q is proportional to the amount of hydroquinone that forms on the surface of the C supports due to degradation. For all the catalysts studied, the HQ/Q peak did not form. This shows that the protocol used in the intentional degradation of the catalysts results in minimal C corrosion and that the predominant cause of ECSA reduction is Pt degradation. Degradation in fuel cells is known to occur via processes that include Pt dissolution, Ostwald ripening, agglomeration, particle detachment as well as support corrosion [54]. The degradation of Pt was observed as a decline in normalized ECSA % as load cycling was carried out. During the initial 100 cycles, there was an observed increase in ECSA for the Pt/BNHCSs while the other catalysts showed a decline in ECSA. The ECSA increase could be attributed to the cleaning effect of the cycling protocol which resulted in more Pt active sites being exposed. In addition, roughening of the surface of the Pt due to initial Ostwald ripening led to a rougher Pt surface with a higher surface area compared to the initial surface area [55]. During the initial 1000 potential cycles, the Pt/BNHCSs catalyst lost only 0.2 % of the initial ECSA (Table S4). The biggest loss occurred for the commercial benchmark Pt/C catalyst which lost about 24 % of the initial ECSA. The Pt/BHCSs catalyst had the second least reduction in ECSA of about 6 %, again much less than found for the Pt/C catalyst (Table 5). The observed durability was attributed to the structure of the supports used for these two catalysts where there is a correlation between degradation and the structure of the supports used. During the initial 1000 durability cycles, the catalyst/support system with the smallest change in textual properties had the highest ECSA loss whereas those with large changes in textual properties (Table S2), had small losses in ECSA. The carbon support used in the commercial benchmark catalyst material had a BET surface area of 250 m^2 g^{-1} whereas when loaded with Pt the BET surface area was reduced to about 220 m^2 g^{-1}. This represents a relatively small change in surface area of about 12% compared to the other catalysts (39 % for Pt/BHCSs; 45 % for Pt/BNHCSs).

From 1000 to 6000 cycles, the highest durability loss occurred in the Pt/BNHCSs catalyst (Table 5 and Table S5). This catalyst system lost about 40.5 % ECSA in this region. As discussed above, it is proposed that pore confinement of Pt is highest in this catalyst system (Pt/BNHCSs), therefore suggesting that the durability loses is due to other properties and is attributed to the small initial particle size for the Pt/BNHCSs (3.8 nm) due to N_2 doping.

After 5000 cycles of durability testing, the ECSA losses decreased for most catalysts (Table 5 and Table S6). During the last 1000 cycles, the highest ECSA loss was observed for the commercial benchmark Pt/C catalyst with a loss in ECSA of 6.7 %. This was followed by the Pt/BNHCSs with an ECSA loss of 3.0 %. The Pt/BHCSs catalysts showed a minimal 0.8 % loss in ECSA. The small losses in ECSA for all the catalysts is attributed to the increased Pt size arising from the durability cycling. After durability studies, the bigger Pt particles due to durability cycling, that are not pore confined, have less surface energy to agglomerate or dissolve resulting in an approximately constant ECSAs [56]. This effect works in collaboration with the Pt confined in the pores of the supports which is prevented from undergoing degradation as explained previously.

After 6000 cycles, the Pt/BHCSs catalyst retained the highest ECSA (Table 5). The catalyst maintained 65.4 % of the initial surface area. This was followed by the Pt/BNHCSs which retained 59.4 % of the initial ECSA. Even though N-doping caused degradation of the catalysts, the effect was not as strong as the effects due to textual properties that was observed for the commercial benchmark Pt/C where a final ECSA% of 47.6 % was observed. The highly graphitized C of the commercial benchmark catalyst generally has poor contact with the Pt particles due fewer defects compared to the other supports.

Table 5: Loss of ECSA due to durability cycling for the Pt/BHCSs, Pt/BNHCSs and the commercial benchmark Pt/C catalysts

Sample	ECSA% 0 cycles	ECSA% 1000 cycles	ECSA% 5000 cycles	ECSA% 6000 cycles	ECSA % lost
Pt/C	100	76.1	54.3	47.6	52.4
Pt/BHCSs	100	94.5	66.2	65.4	34.6
Pt/BNHCSs	100	99.8	62.1	59.1	37.9

4. Conclusions

Catalysts made from Pt deposited on broken C and N doped C supports (Pt/BHCSs and Pt/BNHCSs) have been prepared. The high surface area and bigger pore widths and volumes enabled Pt pore confinement that led to both excellent activity and catalyst durability. As expected, the Pt nanoparticles were smaller on the N doped and high surface area supports

compared to the pristine supports. XPS analysis confirmed the presence of a range of N groups on the BHNCSs (7.4 at %; pyridinic, pyrrolic, graphitic nitrogen, oxidized nitrogen and pyridyl) that are known to bind to Pt and would have restricted Pt particle growth during deposition. In summary, the new catalysts had small initial Pt particle sizes (3 – 5 nm) and the Pt was placed on a high BET surface area support (755 m^2 g^{-1} and 782 m^2 g^{-1}), with a broken bowl-like shape with a small diameter and a thin shell. This morphology allowed for good connection between the broken shells and for loading of the Pt on both sides of the C. Furthermore, the carbon had pores that were of the correct size to match the Pt particle size that resulted in pore filling by the Pt leading to pore confinement that restricted Pt agglomeration as determined by in-situ XRD studies. Of further importance, it was found that the Pt particle size was similar to the width of both the BHCS and BNHCS shells. This implied that access to the same Pt particle was possible from both sides of the support while a strong interaction of the Pt within the pore occurred. We suspect that this is the key finding that is responsible for the remarkable electrochemical behaviour found for these catalysts.

Even though all the three catalysts studied had similar Pt particle sizes and comparable ECSA, the ORR activity and durability values of the three catalysts were different. The Pt/BHCSs and Pt/BHNCSs showed excellent SA (162 and 303 µA cm^{-2}) and MA (109 and 188 A g^{-1}) values at 0.9 V. These were superior to those of the commercial benchmark Pt/C (107 µA cm^{-2} and 65 A g^{-1}). It appears that the structure of the small broken bowl-like supports, together with the presence of the N dopant, enabled more Pt active sites to be exposed to the oxygen saturated electrolyte for the Pt/BHCSs and Pt/BNHCSs compared to the commercial benchmark Pt/C catalyst resulting in better ORR activity.

ECSA values for the catalysts revealed that the Pt/BHCS (65.4 %) and Pt/NBHCSs (59.1 %) they retained high values even after 6000 cycles. The retention was also superior to that of a commercial benchmark Pt/C (47.6 %). This enhanced durability under potential cycling can also be attributed to the pore size and defect confinement of the Pt and enhanced metal-support interactions.

5. Conflicts of interest

There are no conflicts of interest to declare

6. Acknowledgements

We thank the South Africa Department of Science and Innovation for funding the project through a HySA Catalysis student bursary. Financial support from the University of the Witwatersrand postgraduate merit award is also acknowledged. The authors greatly acknowledge the staff from the microscopy and microanalysis unit at the University of the Witwatersrand and the staff at the Aaron Klug Centre for Imaging and Analysis at the University of Cape Town. The National Institute of Meteorology South Africa (NMISA), for XPS measurements is also acknowledged. We acknowledge the the David Cockayne Centre for Electron Microscopy, University of Oxford for the annular dark field (ADF) - bright-field (BF) -STEM measurements. The Chemical Engineering Department at the University of Cape Town is acknowledged for providing electrochemical equipment and laboratory space.

7. References

(1) H.A. Gasteiger, S.S. Kocha, B. Sompalli, T.F. Wagner, Activity Benchmarks and Requirements for Pt, Pt-Alloy, and Non-Pt Oxygen Reduction Catalysts for PEMFCs. *Applied Catalysis B: Environmental* 56 (**2005)** 9-35

(2) N. Guerrero-Moreno, M. Cisneros-Molina, D. Gervasio, J. F. Pérez-Robles, Approaches to Polymer Electrolyte Membrane Fuel Cells (PEMFCs) and Their Cost, *Renewable and Sustainable Energy Reviews* 52 (**2015)**

(3) W. Chen, J. Huang, J. Wei, D. Zhou, J. Cai, Z. D. He, Y. X. Chen, Origins of High Onset Overpotential of Oxygen Reduction Reaction at Pt-Based Electrocatalysts: A Mini Review. *Electrochemistry Communications* 96 (**2018)**,71 - 76

(4) B. Garland, DOE Fuel Cell Program Durability Technical Targets and Testing Protocols DOE Fuel, *ECS Transactions* 11 (**2007**) 923

(5) A.H.A.M. Videla, L. Zhang, J. Kim, J. Zeng, C. Francia, J. Zhang, S. Specchia. Mesoporous carbons supported non-noble metal Fe–N_X electrocatalysts for PEM fuel cell oxygen reduction reaction. *J Appl Electrochem* 43 (**2013**) 159–169

(6) M.E. Kreider, A. Gallo, S. Back, Y. Liu, S. Siahrostami, D. Nordlund, R. Sinclair, J. K. Nørskov. Precious Metal-Free Nickel Nitride Catalyst for the Oxygen Reduction Reaction. *ACS Appl. Mater. Interfaces* 11 (**2019**) 26863–26871

(7) H. Kwon, M.K. Kabiraz, J. Park, A. Oh, H. Baik, S. Choi, K. Lee. Dendrite-Embedded Platinum–Nickel Multiframes as Highly Active and Durable Electrocatalyst toward the Oxygen Reduction Reaction. *Nano Lett.* 18 (**2018**) 2930–2936

(8) T. Jeon, S.K. Kim, N. Pinna, A. Sharma, J. Park, S.Y. Lee, H.C. Lee, S.W. Kang, H.K. Lee, H.H. Lee. Selective Dissolution of Surface Nickel Close to Platinum in PtNi Nano catalyst toward Oxygen Reduction Reaction. *Chem. Mater.* 28 (**2016**) 1879–1887

(9) H. Kuroki, T. Tamaki, M. Matsumuto, M. Arao, K. Kubobuchi, H. Inai, T. Yamaguchi. Platinum–Iron–Nickel Trimetallic Catalyst with Superlattice Structure for Enhanced Oxygen Reduction Activity and Durability. *Ind. Eng. Chem. Res.* 55 (**2016**) 11458–11466

(10) T. Tanaki, A. Koshiishi, Y. Sugawara, H. Kuroki, Y. Oshiba, T. Yamaguchi. Evaluation of performance and durability of platinum–iron–copper with $L1_0$ ordered face-centered tetragonal structure as cathode catalysts in polymer electrolyte fuel cells. *J Appl Electrochem* 48 (**2018**) 773–782.

(11) D. Banham, S. Ye, K. Pei, J.I. Ozaki, T. Kishimoto, Y. Imashiro, A Review of the Stability and Durability of Non-Precious Metal Catalysts for the Oxygen Reduction Reaction in Proton Exchange Membrane Fuel Cells. *Journal of Power Sources 285* (**2015**) 334-348

(12) M. Yin, J. Xu, Q. Li, J.O. Jensen, Y. Huang, L.N. Cleemann, N. Bjerrum, W. Xing. Highly active and stable Pt electrocatalysts promoted by antimony doped SnO_2 supports for oxygen reduction reactions. *Applied Catalysis B: Environmental* 144 (**2014**) 112–120

(13) J. Wang, G. Yin, Y. Shao, S. Zhang, Z. Wang, Y. Gao, Effect of Carbon Black Support Corrosion on the Durability of Pt/C Catalyst. *Journal of Power Sources*, 171 (**2007)** 331-339

(14) G. Liu, X. Liu, P. Ganesan, B.N. Popov, Development of non-precious metal oxygen-reduction catalysts for PEM fuel cells based on N-doped ordered porous carbon. *Applied Catalysis B: Environmental* 93 (**2009**) 156‑165

(15) P. Hernandez-Fernandez, M. Montiel, P. Ocon, J. L. Gomez de la Fuente, S. Garcia-Rodriguez, S. Rojas, J.L.G. Fierro, Functionalization of multi-walled carbon nanotubes and application as supports for electrocatalysts in proton-exchange membrane fuel cell. *Applied Catalysis B: Environmental* 99 (**2010**) 343–352

(16) Y. Zhou, K. Neyerlin, T. S. Olson, S. Pylypenko, J. Bult, H. N. Dinh, T. Gennett, Z. Shao, R. O'hayre, Enhancement of Pt and Pt-Alloy Fuel Cell Catalyst Activity and Durability via Nitrogen-Modified Carbon Supports. *Energy & Environmental Science* 3 **(2010)** 1437.

(17) J. Liu, W. Li, W, R. Cheng, Q. Wu, J. Zhao, D. He, S. Mu, Stabilizing Pt Nanocrystals Encapsulated in N-Doped Carbon as Double-Active Sites for Catalyzing Oxygen Reduction Reaction. *Langmuir* 35 (**2019)** 2580–2586.

(18) W. Stöber, A. Fink, E. Bohn, Controlled Growth of Monodisperse Silica Spheres in the Micron Size Range. *Journal of Colloid and Interface Science* 26 (**1968)** 62–69.

(19) M. W. Dlamini, T. N. Phaahlamohlaka, D. O. Kumi, R. Forbes, L. L. Jewell, N.J. Coville, Post Doped Nitrogen-Decorated Hollow Carbon Spheres as a Support for Co Fischer-Tropsch Catalysts. *Catalysis Today* 342 (**2020)** 99–110.

(20) R. Mohamed, T. Binninger, P.J. Kooyman, A. Hoell, E. Fabbri, A. Patru, A. Heinritz, T.J. Schmidt. P. Levecque, Facile Deposition of Pt Nanoparticles on Sb-Doped SnO_2 Support with Outstanding Active Surface Area for the oxygen reduction reaction. *Catal. Sci. Technol* 8 (**2018)** 2672-2685

(21) Y. Garsany, O.A. Baturina, K.E. Swider-Lyons, S.S. Kocha, Experimental Methods for Quantifying the Activity of Platinum Electrocatalysts for the Oxygen Reduction Reaction. *Anal. Chem*. 82 (**2010)** 6321–6328

(22) M. Inaba, Durability of Electrocatalysts in Polymer Electrolyte Fuel Cells. *ECS Trans.* 25 (**2009)** 573.

(23) I. Takahashi, S.S. Kocha, Examination of the Activity and Durability of PEMFC Catalysts in Liquid Electrolytes. *Journal of Power Sources* 195 (**2010)** 6312–6322.

(24) Z. Yan, Z. Hu, C. Chen, H. Meng, P.K. Shen, H. Ji, Y. Meng, Hollow Carbon Hemispheres Supported Palladium Electrocatalyst at Improved Performance for Alcohol Oxidation. *Journal of Power Sources* 195 (**2010)** 7146–7151.

(25) A. Sadezky, H. Muckenhuber, H. Grothe, R. Niessner, U. Pöschl, Raman Microspectroscopy of Soot and Related Carbonaceous Materials Spectral Analysis and Structural Information. *Carbon* 43 (**2005)** 1731-1742

(26) S. Chung, D. Shin, M. Choun, S. Kim, S. Yang, M. Choi, J.W. Kim, J. Lee, Improved water management of Pt/C cathode modified by graphitized carbon nanofiber in proton exchange membrane fuel cell. *Journal of Power Sources* 399 (**2018**) 350-356

(27) A.C. Ferrari, Raman Spectroscopy of Graphene and Graphite Disorder, Electron–Phonon Coupling, Doping and Nonadiabatic Effects. *Solid State Communications* 143 (**2007)** 47-57
(28) D. Geng, S. Yang, Y. Zhang, J. Yang, J. Liu, R. Li, T.K. Sham, X. Sun, S. Ye, S. Knights, Nitrogen Doping Effects on the Structure of Graphene. *Applied Surface Science* 257 (**2011)** 9193–9198.
(29) P. Mardle, X. Ji, J. Wu, S. Guan, H. Dong, S. Du, Thin film electrodes from Pt nanorods supported on aligned N-CNTs for proton exchange membrane fuel cells. *Applied Catalysis B: Environmental* 260 (**2020**) 118031
(30) C. Yang, M. Zhou, Q. Xu, Confining Pt Nanoparticles in Porous Carbon Structures for Achieving Durable Electrochemical Performance. *Nanoscale* 6 (**2014)** 11863–11870.
(31) C. Galeano, J.C. Meier, V. Peinecke, H. Bongard, I. Katsounaros, A.A. Topalov, A. Lu, K.J.J. Mayrhofer, F. Schüth, Toward Highly Stable Electrocatalysts via Nanoparticle Pore Confinement. *J. Am. Chem. Soc*. 134 (**2012)** 20457–20465
(32) A.M. Jauhar, Z. Ma, M. Xiao, G. Jiang, S. Sy, S. Li, A. Yu, Z. Chen, Space-Confined Catalyst Design toward Ultrafine Pt Nanoparticles with Enhanced Oxygen Reduction Activity and Durability. *Journal of Power Sources* 473 (**2020)** 228607.
(33) Y. Lv, Y. Fang, Z. Wu, X. Qian, Y. Song, R. Che, A.M. Asiri, Y. Xia, B. Tu, D. Zhao, In-Situ Confined Growth of Monodisperse Pt Nanoparticle@Graphene Nanobox Composites as Electrocatalytic Nanoreactors. *Small* 11 (**2015)** 1003–1010.
(34) L. C. Gontard, R. E. Dunin-Borkowski, M.H Gass, A.L. Bleloch, D. Ozkaya, Three-Dimensional Shapes and Structures of Lamellar-Twinned Fcc Nanoparticles Using ADF STEM. *J Electron Microsc (Tokyo)* 58 (**2009)** 167–174.
(35) Z. Duan, G. Wang, Comparison of Reaction Energetics for Oxygen Reduction Reactions on Pt (100), Pt (111), Pt/Ni (100), and Pt/Ni (111) Surfaces: A First-Principles Study. *J. Phys. Chem. C* 117 (**2013)** 6284–6292.
(36) C. Tang, J. Shi, X. Bai, A. Hu, N. Xuan, Y. Yue, T. Ye, B. Liu, P. Li, P. Zhuang, J. Shen, Y. Liu, Z. Sun, CO_2 Reduction on Copper's Twin Boundary. *ACS Catal* 10 (**2020)** 2026–2032.
(37) Y. Liu, B. Huang, X. Zhang, X. Huang, Z. Xie, In-situ fabrication of nitrogen-doped carbon nanosheets containing highly dispersed single iron atoms for oxygen reduction reaction, *Journal of Power Sources* 412 (**2019**) 125-133
(38) G. Prieto, M. Shakeri, K.P. de Jong, P.E. de Jongh, Quantitative Relationship between Support Porosity and the Stability of Pore-Confined Metal Nanoparticles Studied on CuZnO/SiO_2 Methanol Synthesis Catalysts. *ACS Nano* 8 (**2014)** 2522–2531.
(39) Y. Ma, C. Ricciuti, T. Miller, J. Kadlowec, H. Pearlman, Enhanced Catalytic Combustion Using Sub-Micrometer and Nano-Size Platinum Particles. *Energy and Fuels* 22 (**2008)** 3695–3700.
(40) Z.Q. Li, C.J. Lu, Z.P. Xia, Y. Zhou, Z. Luo, X-Ray Diffraction Patterns of Graphite and Turbostratic Carbon. *Carbon* 45 **(2007)** 1686-1695
(41) S.W. Jung, B.N. Popov, Improved Durability of Pt Catalyst Supported on N-Doped Mesoporous Graphitized Carbon for Oxygen Reduction Reaction in Polymer Electrolyte Membrane Fuel Cells. *Carbon* 42 (**2017)** 265–274.
(42) Y. Chen, J. Wang, H. Liu, R. Li, X. Sun, S. Ye, S. Knights, Enhanced Stability of Pt Electrocatalysts by Nitrogen Doping in CNTs for PEM Fuel Cells. *Electrochemistry Communications* 11 (**2009)** 2071–2076.
(43) H. Borchert, E.V. Shevchenko, A. Robert, I. Mekis, A. Kornowski, G. Grübel, H. Weller, Determination of Nanocrystal Sizes: A Comparison of TEM, SAXS, and XRD Studies of Highly Monodisperse CoPt3 Particles. *Langmuir* 21 (**2005)** 1931–1936.

(44) Y. Zhou, K.S. Neyerlin, T. Olson, S. Pylypenko, J.N. Bult, H. Dinh, T. Gennett, Z. Shao, R. O'Hayre, Enhancement of Pt and Pt-Alloy Fuel Cell Catalyst Activity and Durability via Nitrogen -Modified Carbon Supports. *Energy & Environmental Science* 3 (**2010)** 1437–1446

(45) H.S. Lee, G. Young Baek, I. Hwang, C. Jung, J. Choi, Preparation of Porous Carbon Films from Polyacrylonitrile by Proton Irradiation and Carbonization. *Radiation Physics and Chemistry* 141 (**2017)** 369-374

(46) R. Yu, L. Chen, Q. Liu, J. Lin, K.L. Tan, S.C. Ng, H.S.O. Chan, G.Q. Xu, T.S.A. Hor, Platinum Deposition on Carbon Nanotubes via Chemical Modification. *Chemistry of Materials* 10 (**1998)** 718–722.

(47) Y. Wang, Y. Shao, W.D. Matson, J. Li, Y. Lin, Nitrogen-Doped Graphene and Its Application in Electrochemical Biosensing. *ACS Nano* 4 (**2010)** 1790–1798

(48) C. Jackson, G. Smith, D. Inwood, A.S. Leach, P.S. Whalley, M. Callisti, T. Polcar, A.E. Russell, P. Levecque, D. Kramer, Electronic metal-support interaction enhanced oxygen reduction activity and stability of boron carbide supported platinum. *Nat Commun* 8 (**2017)** 15802

(49) G. Liu, X. Li, P. Ganesan, B. N. Popov, Development of non-precious metal oxygen-reduction catalysts for PEM fuel cells based on N-doped ordered porous carbon. *Applied Catalysis B: Environmental* 93 (**2009**) 156‑165

(50) V.S. Bagotsky, *Fuel Cells: Problems and Solutions*; John Wiley & Sons, second edition, **2012**, chapter 12, Electrocatalysis, page 210

(51) G. Wang, Z. Yang, Y. Du, Y. Yang, Programmable Exposure of Pt Active Facets for Efficient Oxygen Reduction. *Angewandte Chemie International Edition* 58 (**2019)** 15848–15854.

(52) S. Jiang, L. Zhu, Y. Ma, X. Wang, J. Liu, J. Zhu, Y. Fan, Z. Zou, Z. Hu, Direct Immobilization of Pt–Ru Alloy Nanoparticles on Nitrogen-Doped Carbon Nanotubes with Superior Electrocatalytic Performance. *Journal of Power Sources* 195 (**2010)** 7578–7582.

(53) H. Lv, S. Mu, N. Cheng, M. Pan, Nano-silicon carbide supported catalysts for PEM fuel cells with high electrochemical stability and improved performance by addition of carbon. *Applied Catalysis B: Environmental* 100 (**2010**) 190–196

(54) X. Wang, W. Li, Z. Chen, M. Waje, Y. Yan, Durability investigation of carbon nanotube as catalyst support for proton exchange membrane fuel cell, *Journal of Power Sources* 158 (**2006**) 154-159

(55) J. Zhao, A. Manthiram, Pre leached Pd–Pt–Ni and binary Pd–Pt electrocatalysts for oxygen reduction reaction in proton exchange membrane fuel cells. *Applied Catalysis B: Environmental* 101 (**2011**) 660–668

(56) T. Nishikawa, N. Aoki, H. Inoue, H. Daimon, M. Inaba, Improvement of Durability in Au Core/Pt Shell Structured Catalyst with PtRu Shell Formation. *Meet. Abstr* 15 (**2013)** *MA2013-02* 1520.